Performance of Wendelstein 7-X stellarator plasmas during the first divertor operation phase

R. C. Wolf[1], A. Alonso[2], S. Äkäslompolo[1], J. Baldzuhn[1], M. Beurskens[1], C. D. Beidler[1], C. Biedermann[1], H.-S. Bosch[1], S. Bozhenkov[1], R. Brakel[1], H. Braune[1], S. Brezinsek[3], K.-J. Brunner[1], H. Damm[1], A. Dinklage[1], P. Drewelow[1], F. Effenberg[4], Y. Feng[1], O. Ford[1], G. Fuchert[1], Y. Gao[3], J. Geiger[1], O. Grulke[1], N. Harder[5], D. Hartmann[1], P. Helander[1], B. Heinemann[5], M. Hirsch[1], U. Höfel[1], C. Hopf[5], K. Ida[6], M. Isobe[6], M. W. Jakubowski[1], Y. O. Kazakov[7], C. Killer[1], T. Klinger[1], J. Knauer[1], R. König[1], M. Krychowiak[1], A. Langenberg[1], H. P. Laqua[1], S. Lazerson[8], P. McNeely[1], S. Marsen[1], N. Marushchenko[1], R. Nocentini[5], K. Ogawa[6], G. Orozco[5], M. Osakabe[6], M. Otte[1], N. Pablant[8], E. Pasch[1], A. Pavone[1], M. Porkolab[9], A. Puig Sitjes[1], K. Rahbarnia[1], R. Riedl[5], N. Rust[1], E. Scott[1], J. Schilling[1], R. Schroeder[1], T. Stange[1], A. von Stechow[1], E. Strumberger[1], T. Sunn Pedersen[1], J. Svensson[1], H. Thomson[1], Y. Turkin[1], L. Vano[1], T. Wauters[7], G. Wurden[10], M. Yoshinuma[6], M. Zanini[1], D. Zhang[1], and the Wendelstein 7-X Team*

[1] Max-Planck-Institut für Plasmaphysik, Wendelsteinstrasse 1, 17491 Greifswald, Germany
[2] Laboratorio Nacional de Fusión, CIEMAT, Avenida Complutense, 40, 28040, Madrid, Spain
[3] Research Center Jülich, Institute for Energy and Climate Research Plasma Physics, Wilhelm-Johnen-Strasse, 52428 Jülich, Germany
[4] University of Wisconsin Madison, Engineering Drive, Madison, WI 53706, United States of America
[5] Max-Planck-Institut für Plasmaphysik, Boltzmannstrasse 2, 85748 Garching, Germany
[6] National Institute for Fusion Science, 322-6 Oroshicho, Toki, Gifu Prefecture 509-5202, Japan
[7] Laboratory for Plasma Physics, LPP-ERM/KMS, Avenue de la Renaissance 30, B-1000 Brussels, Belgium
[8] Princeton Plasma Physics Laboratory, 100 Stellarator Rd, Princeton, NJ 08540, United States of America
[9] Massachusetts Institute of Technology, 77 Massachusetts Ave, Cambridge, MA 02139, United States of America
[10] Los Alamos National Laboratory, Los Alamos, NM 87544, United States of America

Abstract

Wendelstein 7-X is the first comprehensively optimized stellarator aiming at good confinement with plasma parameters relevant to a future stellarator power plant. Plasma operation started in 2015 using a limiter configuration. After installing an uncooled magnetic island divertor, extending the energy limit from 4 to 80 MJ, operation continued in 2017. For this phase, the electron cyclotron resonance heating (ECRH) capability was extended to 7 MW, and hydrogen pellet injection was implemented. The enhancements resulted in the highest triple product (6.5×10^{19} keV m^{-3} s) achieved in a stellarator up to now. Plasma conditions ($T_e(0) \approx T_i(0) \approx 3.8$ keV, $\tau_E > 200$ ms) already were in the stellarator reactor-relevant ion-root plasma transport regime. Stable operation above the 2nd harmonic ECRH X-mode cut-off was demonstrated, which is instrumental for achieving high plasma densities in Wendelstein 7-X. Further important developments include the confirmation of low intrinsic error fields, the observation of current-drive induced instabilities, and first fast ion heating and confinement experiments. The efficacy of the magnetic island divertor was instrumental in achieving high performance in Wendelstein 7-X. Symmetrization of the heat loads between the ten divertor modules could be achieved by external resonant magnetic fields. Full divertor power detachment facilitated the extension of high power plasmas significantly beyond the energy limit of 80 MJ.

*For Wendelstein 7-X Team see author list: T. Klinger et al, Nucl. Fusion 59 (2019) 112004, doi.org/10.1088/1741-4326/ab03a7

Introduction

The two most established concepts for magnetic confinement fusion are the tokamak and the stellarator (see e.g. [1]). In both kinds of devices, the magnetic field lines trace out toroidal surfaces, but their necessary twist (rotational transform) is produced in different ways. In the tokamak, it requires a strong toroidal plasma current, which is normally generated by transformer action of a central solenoid. In a steady-state power plant, it would have to be achieved by other methods (see e.g. [2]), which generally require high levels of recirculating power. The largest tokamak under construction, ITER [3], will thus only operate for about 5 minutes in its standard plasma scenario.

In stellarators, coils surrounding the plasma generate rotational transform without requiring plasma currents [4]. This type of device is therefore inherently stationary. The net toroidal current tends to be much smaller than that in tokamaks and only exists insofar that it is arises spontaneously by plasma transport processes (bootstrap current) or the heating systems (neutral-beam injection or high-frequency waves). Current-driven instabilities and plasma current disruptions are generally not a concern, and the toroidal current does not govern the density limit on plasma operation, as is the case in tokamaks with the Greenwald limit [5].

However, a drawback of stellarators is that the toroidal symmetry present of the tokamak cannot be maintained. The consequences for plasma transport are considerable. In both tokamaks and stellarators, the magnetic field strength varies along the field lines, which leads to particle trapping in local magnetic wells. In the tokamak, the collisionless orbits of trapped particles are well confined within the plasma, but in stellarators they are not. Accordingly, neoclassical transport theory, which accounts for the geometry of particle orbits and Coulomb collisions, predict large energy losses in most stellarators even in the absence of plasma turbulence. Fortunately, these losses can be reduced dramatically by optimizing the geometry of the magnetic field [6,7]. This has been done in the Wendelstein 7-X stellarator (W7-X), which was designed to have low neoclassical transport, small bootstrap current, robust magnetic-field equilibrium and, yet, reasonably simple modular field coils [8, 9].

The objective of W7-X is to demonstrate that this theoretically based optimization works in practice, so that plasma properties that extrapolate to power plant requirements can be reached in a stellarator. Specifically, a triple product ($n \cdot T \cdot \tau_E$) comparable to tokamaks of similar size should be achievable in conditions approaching steady-state. High-power operation of W7-X will be limited (mainly by the cooling plant) to 30 minutes, which is several orders of magnitude longer than most characteristic time scales of the plasma, such as the confinement time, the fast-ion slowing-down time or the L/R-time (L is the plasma inductance and R the electrical resistance). The latter describes the time scale on which the toroidal plasma current settles down to a stationary equilibrium. Moreover, for studying plasma-wall interaction, a discharge duration of 30 minutes is a big step forward as the time-integrated heat and particle fluxes reaching the plasma facing components will increase by orders of magnitude compared to a plasma only lasting a few seconds.

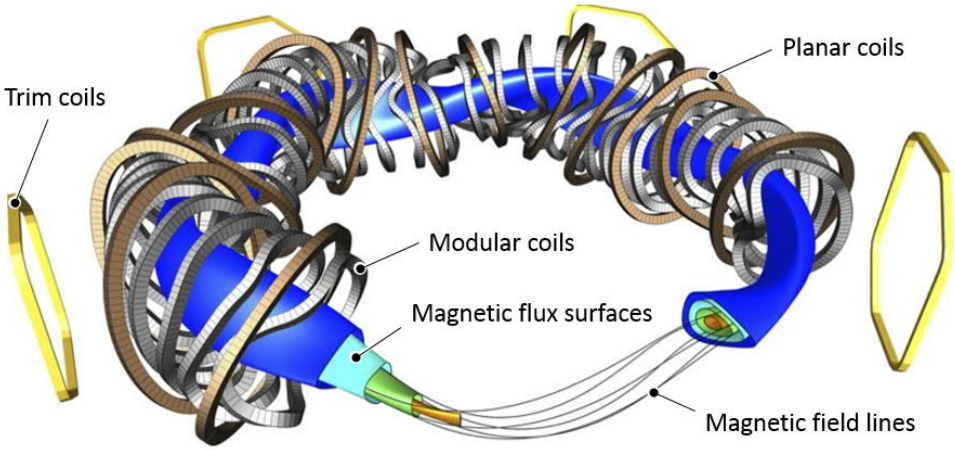

Figure 1. Coil arrangement of W7-X, showing the shaped modular coils, the planar coils (both superconducting) and four (out of five) trim coils (normally conducting), which are used to correct the intrinsic error fields. Selected magnetic flux surfaces and in the foreground magnetic field lines are also illustrated (for illustration purposes, the magnetic field coils in the foreground are cut away; reproduced from [42] with the permission of Springer Nature).

Seven optimization criteria form the basis of the W7-X design [10]: Closed magnetic flux surfaces and small error fields, good equilibrium properties up to volume averaged β-values of $\langle\beta\rangle = 5\%$, MHD stability up to $\langle\beta\rangle = 5\%$, reduced neoclassical transport of the thermal plasma, improved confinement of fast ions, small toroidal bootstrap current and feasible modular coils. Minimizing the Shafranov-shift is expected to lead to good equilibrium properties. In stellarators, the Shafranov-shift, associated with the Pfirsch-Schlüter balancing currents, leads to an increasing ergodization of the magnetic field lines and thus effectively to a loss of confinement volume. Together with the requirement to minimize the bootstrap current, the overall approach is to minimize all plasma currents, except the diamagnetic current, which is an intrinsic property of any magnetized plasma. This means that increasing the plasma pressure or β has only a limited effect on the magnetic field. Solving this complex optimization problem was only possible with the help of the most advanced supercomputers, which became available at the time between the late nineteen seventies and the early nineteen nineties [11].

Together with the question of the optimum size of such an experiment and the requirement to sustain a high-performance plasma over many minutes, the optimization led to a device with 50 modular superconducting coils, a major radius of 5.5 m, an average minor radius of 0.55 m (corresponding to a plasma volume of 30 m^3) and a magnetic field on the magnetic axis of 2.5 T [12]. Half a meter minor radius is considered sufficiently large for a plasma, which is not governed by edge effects and wall recycling, and for which the expected radial transport losses can achieve fusion relevant plasma temperatures and densities in the range of several keV and 10^{20} m^{-3}, respectively. The 50 modular coils consist of five different coil types arranged in five magnetic field modules, which in the toroidal direction repeat the same magnetic field structure five times. Broadly speaking, W7-X consists of five toroidally linked magnetic mirrors. In addition, 20 planar superconducting coils mounted over the modular coils produce vertical and toroidal field components, allowing the radial adjustment of the plasma column and a modification of the rotational transform. Figure 1 shows the different coil types

and the shape of the resulting magnetic flux surfaces. Depending on the ratios of the electrical current of the magnetic field coils, many different magnetic field configurations can be realized [13]. Balancing the benefit of a strong magnetic field on plasma confinement and the requirement to take up the magnetic field forces by a suitable coils support structure, an average magnetic field of 2.5 T on the magnetic axis was chosen.

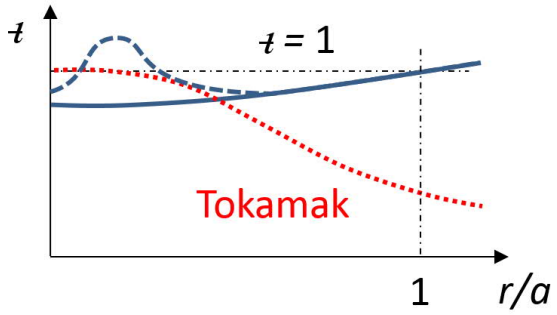

Figure 2. The approximate profile of the rotational transform, ι, of W7-X (solid blue line) is compared with the typical ι-profile of a tokamak (r/a is the normalized minor radius of the plasma). Since in a stellarator the poloidal field is mainly produced by the coils, ι drops from the plasma boundary towards the plasma center. The strong toroidal plasma current in a tokamak leads to an opposite behavior. Also shown is the effect of slightly off-central electron-cyclotron current drive (ECCD), applied in the direction, which increases the rotational transform (dashed blue line). Due to the strong localization of ECCD, the ι-profile can cross $\iota = 1$, forming two major resonances during the current diffusion process.

This choice had a direct impact on the design of the main heating system. From the beginning, the development and construction of an electron-cyclotron-resonance heating (ECRH) facility, capable of heating the plasma over 30 minutes, was an integral part of the W7-X project [14]. The facility consists of ten 140 GHz gyrotrons, each delivering up to 1 MW of microwave power. 140 GHz corresponds to the 2nd harmonic electron-cyclotron frequency at 2.5 T. The 1st harmonic cannot be used, since for all interesting plasma densities the corresponding frequency lies below the cut-off density. Gaussian optics consisting of 18 water-cooled mirrors transmit the power from the gyrotrons to the launchers installed inside the vacuum vessel of W7-X. The overall transmission losses are only about 6% [15]. The launchers use movable mirrors near the plasma (front steering concept) for adjusting the deposition position in the plasma or producing current drive. Moreover, W7-X is equipped with two remote steering launchers, which use specially designed wave-guides and mirrors outside the plasma vessel for steering the microwave beams [16]. The main advantage of these launchers is that they do not need any moveable parts near the plasma and that an opening of ~50 cm^2 is sufficient to inject 1 MW of heating power. In W7-X ECRH is used for both generating and heating of the plasma. Up to now, the ECRH system of W7-X delivered a maximum power of just above 7 MW to the plasma. The longest plasmas sustained were 30 sec at 5 MW and 100 sec at 2 MW.

A very special property of W7-X, which is closely related to the magnetic field configuration, is the magnetic island divertor. The basic concept was first tested in the predecessor experiment Wendelstein 7-AS [17, 18]. In W7-X, a rotational transform of $\iota = 1$ at the plasma boundary combined with low magnetic shear produces large magnetic islands [19]. While the low-order rational value of ι

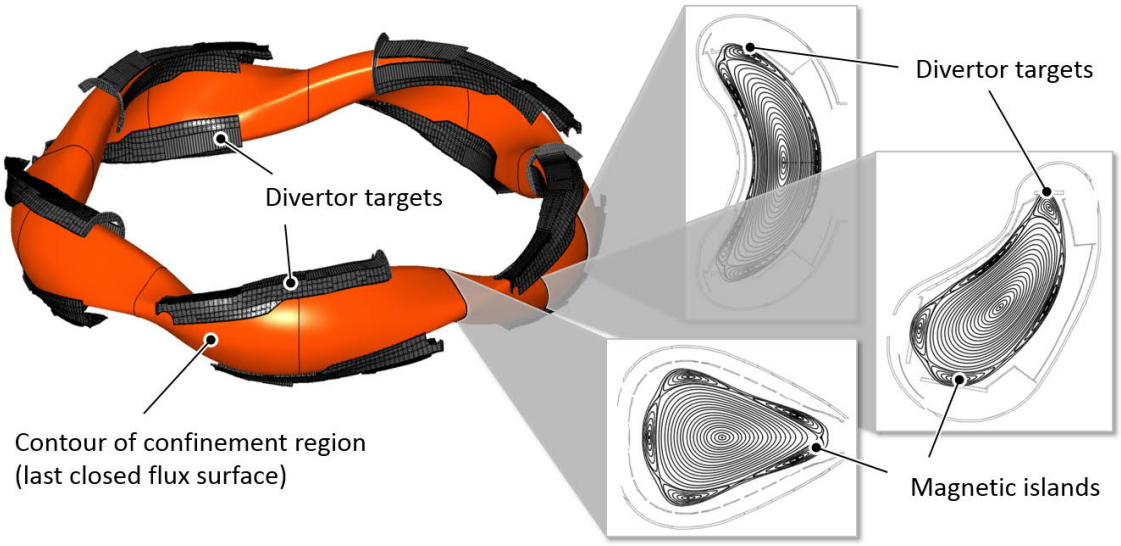

Figure 3. The plasma contour (last closed flux surface) is shown together with the contours of the in-vessel components including the divertor targets. The targets, arranged in ten divertor modules, follow the helicity of the magnetic islands. The three poloidal cross-sections on the right correspond to different toroidal positions (covering an angular range of 36°). Shown are closed magnetic flux surfaces and the magnetic islands (representing the Poincaré plots of the magnetic field lines on those surfaces), and the divertor targets intersecting the magnetic islands.

is responsible for the formation of the islands (with a helicity corresponding to a ratio of toroidal to poloidal mode numbers of n/m = 5/5 = 1), the low magnetic shear ensures that the rotational transform changes only slightly around the resonance, producing islands which are large enough to separate the confinement region from the wall surrounding the plasma. The profile of the rotational transform of W7-X and for comparison a typical tokamak profile are illustrated in Figure 2. The poloidal periodicity of the islands can be varied by shifting the resonance to values slightly above or below one (high- or low-ι cases) [13]. Figure 3 illustrates the island divertor concept. A divertor configuration is achieved if the islands are intersected by target plates, producing a scrape-off layer region, which forms the boundary between the confinement region (defined by closed magnetic field lines lying on flux surfaces) and the target surfaces. Plasma particles, which by radial transport cross the last closed flux surface and thus leave the confinement region, flow along the open magnetic field lines onto the divertor targets. Since the magnetic field lines in the scrape-off layer, which approach the last closed flux surface, only connect to certain wall regions, the target plates do not have to cover the whole plasma surface. Unlike the poloidal divertor in tokamaks, it is not necessary to have continuous targets in the toroidal (or in case of a stellarator helical) direction. Another major difference to tokamaks is that the magnetic field line connection lengths, which are an important parameter determining the width of the power deposition on the divertor targets, are an order of magnitude larger in the magnetic island divertor [20, 21, 22, 23]. Potentially, this leads to a wider spreading of the power reaching the targets and thus to lower peak heat fluxes. A disadvantage of the island divertor, however, is its sensitivity to toroidal plasma currents and magnetic field errors. Since toroidal currents change ι, they must be kept small or their effect has to be compensated by current drive [24]. This is why the minimization of the bootstrap current is part of the W7-X optimization. Imperfections of the magnetic field in form of small deviations from the specified field configuration have detrimental effects on the

island divertor if the associated field errors are resonant to $\iota = 1$. In this case, substructures form inside the islands, which lead to an uneven power distribution between the divertor modules [25, 26]. Using field line diffusion calculations, a resonant error field of $\Delta B_{11}/B = 10^{-4}$ (where the indices of ΔB refer to the poloidal and toroidal mode number of the error field) results in re-distribution of the power, which corresponds to an increase of the peak heat flux compared to the average by a factor of up to two [27]. This assumes a field line diffusion coefficient (defined as the ratio of perpendicular diffusion to parallel flow velocity) of $\sim 10^{-6}$ m^2/m. Higher values would lead to a wider spreading of the strike lines on the divertor targets and, thus, to a reduced imbalance of the heat fluxes. One of the objectives of the so-called trim coils (see Figure 1) [28, 29] is the compensation of residual error fields, aiming toward a near-uniform distribution of the heat fluxes between the divertor modules.

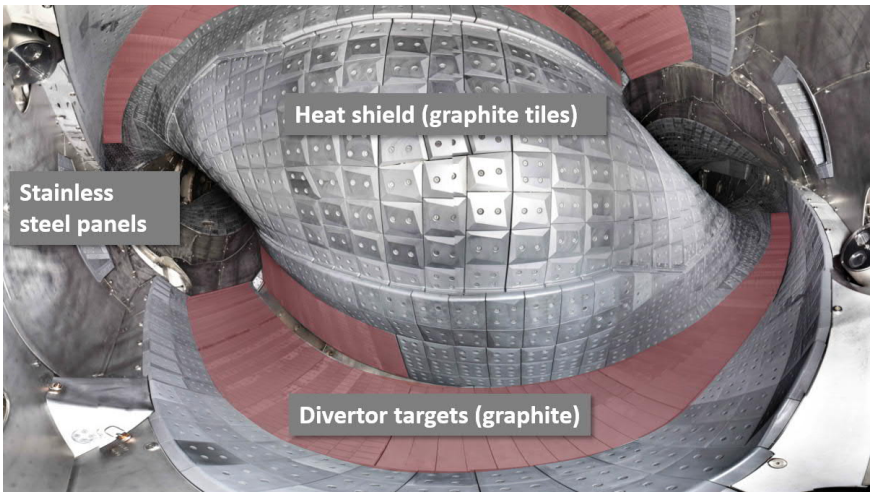

Figure 4. Fisheye view into the plasma vessel of W7-X. The photograph was taken after the installation of the uncooled divertor (reproduced from [40] with the permission of IEEE) plasma facing components mainly consist of three types. The stainless steel panels are not in direct contact with the plasma and are designed for heat fluxes of up to 200 kW/m^2. The graphite heat shield is designed for intermediate heat fluxes, with peak heat loads of up to 500 kW/m^2. The divertor targets, designed for peak heat fluxes of 10 MW/m^2, dissipate the main convective load from the plasma. Diagnostics and other in-vessel installations, depending on their position, must conform with these design values.

Construction of the basic device was completed in 2014 [30]. After first commissioning [31], first plasma was achieved at the end of 2015 [32, 33, 34]. Following a staged approach, in-vessel components, plasma diagnostics and heating systems are being successively completed or upgraded [35]. This concerns in particular the heat exhaust inside the plasma vessel. During the first experimental campaign (OP1.1, 2015/2016), W7-X was equipped with five uncooled inboard graphite limiters, restricting the integrated heating power of one plasma pulse to 4 MJ [36]. For the second and third campaigns (OP1.2a, 2017 and OP1.2b, 2018) ten uncooled graphite divertor modules were introduced (the so-called test divertor unit [37], increasing the energy limit to 80 MJ, which at the end of the third campaign was extended to 200 MJ. The test divertor unit had the exact shape of the actively cooled high-heat flux divertor, the installation of which started end of 2018. The high-heat flux divertor is made of water cooled CuCrZr-elements covered with carbon-fiber-composite (CFC) material [38, 39] and is designed for steady-state heat fluxes up to 10 MW/m^2. Including active cooling of all in-vessel

components and cryo-pumps these upgrades will prepare W7-X for long-pulse operation. In a first step (starting in 2021) a pulse energy of 1 GJ is envisaged, eventually approaching 18 GJ, which at 10 MW of heating power corresponds to plasmas lasting 30 minutes. This paper focuses on results achieved during the first divertor operation (during OP1.2a and OP1.2b) using the uncooled test divertor. Figure 4 shows a fisheye view into the plasma vessel explaining the different wall elements including the divertor targets [40]. The main objective of the last two campaigns was the preparation of long-pulse operation (up to 30 minutes). The experience gained during these two campaigns is aiming at a safe and efficient start of the campaign in 2021.

Performance during first divertor operation

This section is structured along the optimization criteria, which form the basis of the W7-X design. We will try to give first answers as to what extent characteristics of the optimization have already been observed. Observing the energy limit of 80 MJ, the heat exhaust through the uncooled divertor did not pose any limits. Achievements of the divertor operation are discussed in the last subchapter.

Closed magnetic flux surfaces and small error fields

In stellarators, the vacuum magnetic field is already sufficient to provide a force equilibrium, which is capable of confining a plasma. In W7-X, the minimization of the plasma currents means that the modification of the vacuum field with increasing β is comparatively small. Thus, measuring the magnetic flux surfaces in vacuum already delivers crucial information about the quality of the magnetic field. In W7-X, an electron beam technique was employed to visualize the magnetic field lines and the corresponding flux surfaces in vacuum [41]. Depending on the adjustment of the rotational transform, magnetic islands were also observed. For various magnetic field configurations and field strengths, nested magnetic flux surfaces could be clearly identified. The sensitivity was high enough to provide evidence for the flattening of the modular coils caused by the magnetic forces as the magnetic field increases [41].

n/m of error field	error field amplitude $\Delta B/B$	
½	$< 5.4\times10^{-6}$	
1/1	$\approx 8\times10^{-5}$	from magnetic axis shift
1/1	$\approx 5\times10^{-5}$	from trim coil compensation

Table 1. Overview of error field measurements using different techniques.

By making use of the sensitivity of particular ι-values to magnetic error fields, the error fields could be inferred from the electron beam technique. At the beginning of the first experimental campaign an $\iota = ½$ configuration was used to measure the intrinsic n/m = 2/1 error (and its toroidal phase angle) confirming the high precision with which W7-X was built [42, 43]. More interesting, however, is the n/m = 1/1 error, since it has a direct impact on the divertor performance. The employed method compares the measured position of the flux surfaces (represented by the magnetic axis) with the calculated position of the ideal flux surfaces, unperturbed by fabrication and positioning errors of the coils. Thereby, the spatial shift of the magnetic axis as ι on the magnetic axis approaches one (high-ι configuration) is a direct measure of the magnetic field error [44] (2nd line in the table 1). In a second step, the trim coils were applied in a configuration with $\iota = 1$ at the plasma boundary. The trim coil currents required for the suppression of the B_{11} error field induced magnetic islands provides another measurement of the magnetic field error (3rd line in the table). Table 1 summarizes the outcome of the different measurements of the magnetic field errors. A crucial result is that 1/1 error field is below 10^{-4}

meeting the design requirements of W7-X. A different more indirect approach to assess magnetic error fields is to look at the effect they have on the symmetry of the heat load distribution between the different divertor modules. Measurements of the heat load distribution using the thermocouples inside the divertor tiles basically confirmed the high accuracy to which W7-X was built [29].

Good equilibrium properties and reduced collisional transport of the thermal plasma

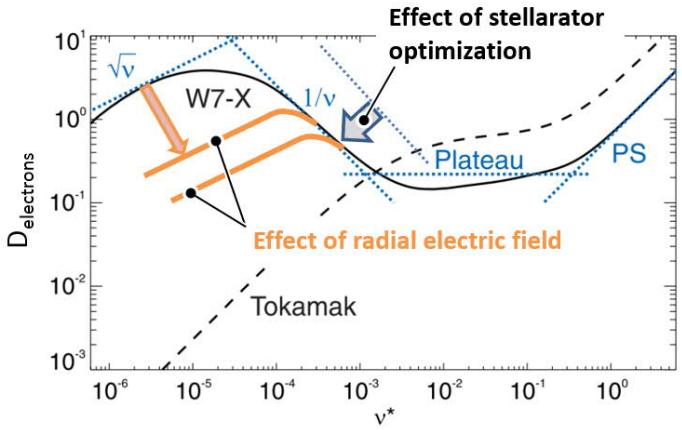

Figure 5. Dependence of the radial transport coefficients as a function of plasma collisionality, comparing stellarator (W7-X: black solid line) and equivalent tokamak (black dashed line; for the details of the definition of the shown quantities and the underlying figure see [7]; reproduced with the permission of IoP publishing). The effect of radial electric fields and the optimization of the neoclassical transport are illustrated in a qualitative way. The two yellow lines characterize the way the transport coefficients drop with increasing electric field.

Since the achievable β at a given heating power depends on the plasma confinement, the following discussion combines equilibrium and transport effects. To understand the approach achieving high confinement in stellarators, it is important to consider the particular properties of neoclassical transport losses in stellarators. Looking at the dependence of the (mono-energetic) transport coefficient on plasma collisionality [6], the difference between tokamaks and stellarators becomes evident (see Figure 5). At high collisionalities, in the Pfirsch-Schlüter (PS) regime, plasma particles undergo such frequent collisions that they do not complete their large particle drift orbits of the gyro-centers in the inhomogeneous magnetic field. As a result, the details of the magnetic field play a secondary role and tokamak and stellarator transport are similar. With decreasing collisionality the neoclassical transport losses in tokamaks rapidly drops to negligible values, while in stellarators neoclassical transport remains high. As particles complete their orbits several times before they collide, the 3D structure of the magnetic field in stellarators (or the lack of toroidal symmetry) becomes evident, leading to an increase of the neoclassical losses. In tokamaks this is the region where anomalous transport caused by plasma turbulence generally exceeds neoclassical values. In stellarators turbulence is of course also present, however the situation is more complicated, as, depending on the level of optimization, the balance between anomalous and neoclassical transport may change considerably.

The collisionality regime, relevant for the extrapolation to a burning fusion plasma and thus relevant for testing stellarator optimization, is the $1/\nu$-regime. For a device of a given size with a given magnetic

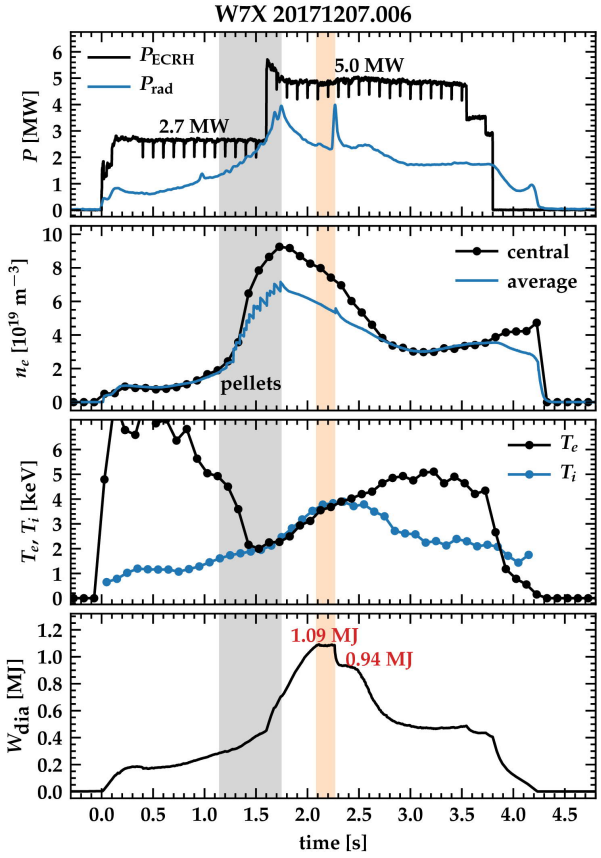

Figure 6. High density, high performance plasma [48]. Shown are the temporal evolution of the heating power, the radiated power, average and central density (from interferometer [49] and Thomson scattering measurements [50], central electron and ion temperatures (from Thomson scattering and X-ray spectroscopy [51], and the plasma energy (from a diamagnetic loop [52]. After injecting pellets (gray shaded area) maximum energy confinement (orange shaded area) was achieved.

field, the transport coefficients scale as $D_{1/\nu} \sim \varepsilon_{eff}^{3/2} T^{7/2}/n$, where T and n are temperature and density of the plasma. Stellarator optimization tries to minimize the effective ripple, ε_{eff} [45, 46], so as to alleviate the effect of the strong temperature dependence. The effective ripple is a figure of merit for the optimization of the neoclassical transport. It accounts for the helical ripple [47], which is composed of the Fourier components of the magnetic field arising from breaking toroidal symmetry. An ε_{eff} of 1% or less is considered sufficient for achieving low enough $1/\nu$-transport. Moreover, high plasma densities and moderate temperatures help to keep the $1/\nu$-transport low. In W7-X, $1/\nu$-transport is of relevance for densities which are high enough to strongly couple electrons and ions, resulting in $T_e \approx T_i$ independent of whether electrons or ions are heated. An additional feature of neoclassical transport in stellarators is the ambipolarity condition, requiring radial electron and ion fluxes to be equal. The resulting radial electric field, E_r, adjusts itself so that the ambipolarity condition is fulfilled. Plasma regions that are governed by $1/\nu$-transport are in the ion-root solution of the ambipolarity condition, corresponding to an E_r which is negative (pointing towards the plasma center). At lower collisionalities, the plasma enters the $\sqrt{\nu}$-regime. In W7-X, this is usually the case at low plasma densities. If in this case the plasma electrons are predominantly heated (as is the case with ECRH), T_e

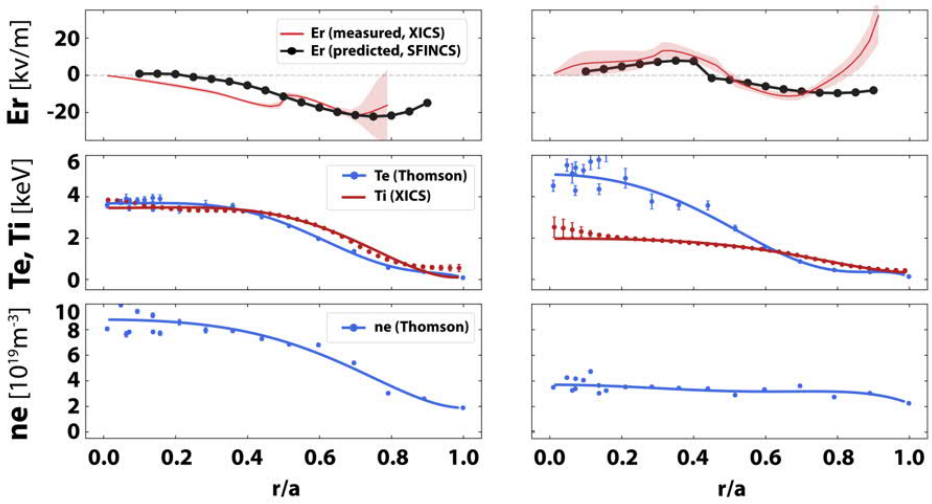

Figure 7. Temperature and density profiles (using the plasma radius, r, normalized to the separatrix radius, a) of the plasma shown in Figure 6 [56]. Electron temperature and density were measured by Thomson scattering. Ion temperature and radial electric field are derived from X-ray spectroscopy [57]. For comparison, also the radial electric field calculated by the SFINCS code [58] is shown. The profiles on the left correspond to the high performance phase (at t ≈ 2.1 sec) when the plasma is in ion-root confinement (negative E_r). The profiles on the right were recorded at a later time (t ≈ 3.5 sec) after the density had dropped and the plasma returned to electron-root confinement in the core of the plasma ($E_r > 0$).

will be considerably larger than T_i. As a result, the electron-root solution of the ambipolarity condition applies, producing a positive E_r. Since this is pointing away from the plasma center, electrons see an attracting force towards the plasma center, effectively reducing their radial transport. In addition, also the transport coefficients are reduced.

Typical high-density ECRH plasmas of W7-X go through several phases (see Figure 6) [48]. Plasma break-down was achieved at low density [49]. The electron temperature [50] increased quickly, while the ions [51], because of the low collisionality, were only weakly heated. The application of pellets increased the density by more than a factor of three and also increased the density peaking. With increasing plasma density and a step-up of the heating power, ion and electron temperature became similar. Once the pellets were consumed, the density started to drop, while the temperatures continued to increase. Interestingly, the plasma energy [52] also continued to increase beyond the pellet phase. The peak performance corresponds to the highest triple product ($n \cdot T_i \cdot \tau_E \approx 6.8 \times 10^{19}$ keV m^{-3} s) observed to date in stellarators or other helical devices [21] [53]. At $\tau_E = 220$ ms, the energy confinement time corresponds to 1.4 times the value of the ISS04 scaling [54]. Eventually, a plasma event, which is visible as a fast drop in the diamagnetic energy and a spike on the radiated power, the origins of which remains to be identified, terminates the high confinement phase.

An important question at this early stage of W7-X experiments is whether stellarator characteristics or even optimization effects have been observed yet. Measurements of the radial electric field clearly show the transition from electron root confinement at low densities and $T_e >> T_i$ to ion root confinement at high densities and $T_e \approx T_i$ [55] giving clear evidence for stellarator behavior. After the termination of the high performance phase, because of the continuing decrease of the density, T_e and T_i became increasingly decoupled and the plasma returned to electron root (see Figure 7) [56, 57, 58].

Moreover, collisionality values already lie in the $1/\nu$-range during the ion root phase of the plasma. The comparison of the calculated neoclassical fluxes with the power balance heat fluxes shows that during the pellet phase (after increasing the heating power) ~25% of the transport losses (at half radius) can be explained by neoclassical losses, while during peak performance this level increases to ~50% [48]. This rise (at constant heating power) can be attributed to the dependence of the neoclassical transport coefficient on temperature and density ($\sim T^{7/2}/n$). While the total energy and both ion and electron temperatures are increasing, the density is decreasing. Assuming that the difference between neoclassical and total heat losses mainly can be attributed to anomalous heat transport, caused by plasma turbulence, the level of turbulence has to decrease. This line of argument is emphasized by the fact that part of the heating power has to go into the energy rise. Moreover, the argument is supported by the measurements of density fluctuations [55] using phase contrast imaging [59]. Figure 8 compares the temporal evolution of the density fluctuation level to the line-integrated density and the diamagnetic energy. During the initial phase of the plasma, including the pellet phase, plasma density, energy and fluctuations more or less rise together. After the pellet injection phase the continuing increase of the plasma energy, without further increasing the heating power, coincides with a significant drop of the turbulent fluctuation level, which persist until the maximum energy is reached. The fact that a record triple product in a device the size of W7-X was achieved with only 5 MW, while the neoclassical transport is only a fraction of the total heat losses, already provides an indication that the optimization of the neoclassical transport is important. A quantitative analysis of the impact of the $\varepsilon_{\mathrm{eff}}$ optimization is still ongoing and will be reported in a later publication. Also important to note is that the characteristic features of an H-mode, namely prominent pedestals of temperature or density at the plasma boundary, have not been observed to date (see also Figure 7).

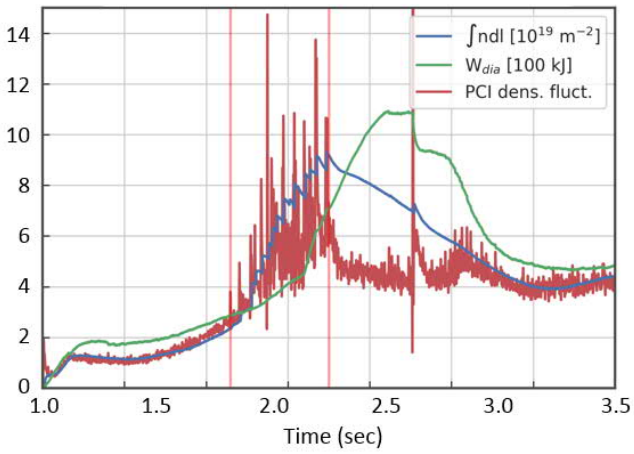

Figure 8. Temporal evolution of line-integrated density, diamagnetic energy and density fluctuation level for the plasma shown in Figure 6 and Figure 7. The turbulent density fluctuations were measured by phase contrast imaging (PCI) along the line-of-sight of an infrared laser [59], covering a frequency range from 20 to 1000 kHz and traversing the plasma mainly in regions of bad curvature.

The plasma shown in Figure 6 and Figure 7 is also one of the examples with the highest volume averaged beta of $\langle\beta\rangle \approx 1\%$. This is not high enough to investigate the stability and equilibrium properties W7-X was designed for. However, the central β close to 4% already is in a range where Shafranov shift and the diamagnetic effect become noticeable. In particular, the diamagnetic drop of

the magnetic field appears as a radial shift of the ECRH resonance away from the magnetic axis [53], which requires an increase of the underlying magnetic field if the ECRH power deposition should be kept in the plasma center during the high performance phase.

The highest performance of W7-X so far was achieved at still moderate densities (line-averaged density below 8×10^{19} m^{-3} and central density below 10^{20} m^{-3}). A further increase of β will require more heating power or a further improvement of the confinement. Since the temperatures during the high performance phase were moderate (just below 4 keV) the neoclassical losses are modest. Because of the strong temperature scaling of the neoclassical losses, the recipe for further increasing plasma energy is to raise both temperature and density. For the W7-X parameters, the standard scheme for plasma break-down and heating with electron-cyclotron-resonance waves is the 2nd harmonic X-mode (X2). The cut-off density for this wave polarization lies at 1.2×10^{20} m^{-3}. Aiming at higher densities, the ECRH facility was designed to also provide 2nd harmonic O-mode (O2). The problem with O2-mode heating is that the plasma absorption is not very efficient, requiring an elaborate multi-pass absorption scheme for efficient heating [15]. In addition, plasma start-up and efficient heating at temperatures much below 3 keV is not possible with O2-heating. This means that dedicated start-up scenarios had to be developed, changing from X2-heating to O2-heating, while maintaining a sufficiently high power level. With the heating power available, it was indeed possible to increase the central plasma density above the X2 cut-off (beyond 1.2×10^{20} m^{-3}) and sustain the plasma purely with O2-heating [60, 53]. At central electron temperatures of 2.9 keV an absorbed power fraction above 80% was possible. Theoretically, the density cut-off for O2-heating lies at 2.4×10^{20} m^{-3}, but practically, the absorption efficiency limits the density to 1.8×10^{20} m^{-3}.

Maximizing the density raises the question of possible density limits. In stellarators the Greenwald density limit observed in tokamaks [5] does not exists. The usual explanation for density limits in stellarators rests upon the radiation losses associated with impurities in the plasma. In this respect W7-X is not an exception. The achievable density in hydrogen plasma clearly shows the expected heating power scaling including the dependence on low-Z impurities [61]. In particular, when wall conditioning with glow discharge cleaning incorporating a mixture of helium and diborane (called boronization) was used, low-Z impurities in the plasma were significantly reduced, resulting in a profound effect on increasing the density limit (at a given heating power). The critical density increased by about a factor of 3, corresponding to a decrease of the low-Z impurity concentration by factors between 5 and 10. At a heating power of 5 MW this meant that line-averaged densities of $\int n_e dl/l \approx 10^{20}$ m^{-3} became accessible. Within the scatter of the data, a dependence on the magnetic field configuration was not observed.

MHD stability

As already explained, the volume-averaged β was not high enough to explore the stability limits, which were part of the optimization procedure [62]. An instability related to the radiation event in the plasma shown in Figure 6, which coincided with the termination of the high-performance phase, could not yet be identified.

However, a very interesting observation is that driving electron-cyclotron-resonance current (ECCD) close to the plasma center induces electron temperature crashes, which are reminiscent of sawtooth oscillation in tokamaks [63] (see Figure 9). These experiments have a particular importance for magnetic field configurations with bootstrap currents large enough to influence the strike line position

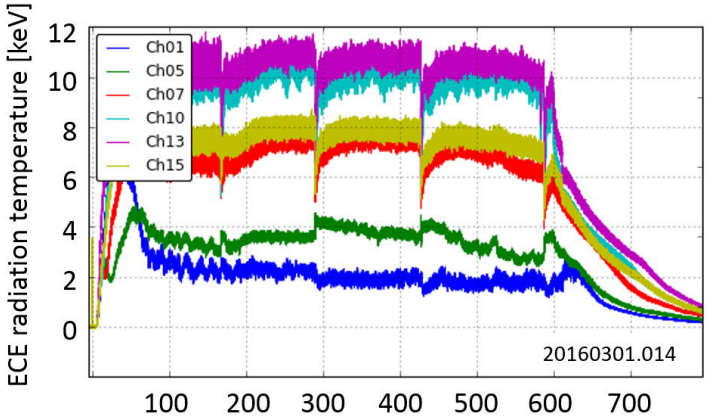

Figure 9. The figure shows recurring oscillations of the ECE radiation temperature, induced by co-ECCD. The measurement channels (Ch1 … Ch15) correspond to different minor radius positions (ordered along the major radius). Ch01 is close to the plasma edge; Ch10 and Ch13 are close to the centre (near the ECRH/ECCD deposition), and Ch15 again lies at a larger minor radius. A (phase) inversion of the heat wave from the plasma core towards the plasma edge, associated with the strong temperature crashes in the plasma centre, is clearly visible between Ch5 and Ch7.

of the divertor (see below). In such cases, ECCD is considered one of the options to control or compensate the effect of the bootstrap current on the divertor performance. Since the highest bootstrap currents are expected for the configurations with the lowest neoclassical transport losses, the application of ECCD might turn out to be a crucial element for achieving high performance operation together with optimal divertor conditions. The main tool to induce such oscillations or crashes is ECCD near the plasma center. A plausible explanation is based on the effect of the current-drive on the ι-profile. Considering the interplay between driven current, formation and decay of shielding currents and the slow diffusion of the current on the skin-time scale [32], locally driven current causes the ι-profile to become non-monotonic. A local maximum or minimum form near the plasma center, depending on whether the driven current increases the helicity of the magnetic field lines (co-current drive) or decrease the helicity (counter-current drive). In case of co-current drive, this means that two major resonances at $\iota = 1$ lying close to each other form (see Figure 2). First estimations with the resistive MHD code CASTROR3D [64] using calculated ι-profiles indicate that double tearing modes maybe responsible for the observed temperature crashes. It is interesting to note, that this would explain the occurrence of the first crash. However, the recurring oscillations need a mechanism, which redistributes current on a fast time scale and which, similar to the sawtooth instability in tokamaks, is associated with magnetic reconnection.

Confinement of fast ions

In a burning fusion plasma, fast ions arise from the fusion reactions. In a D-T-plasma these are the 3.5 MeV α-particles that also need to be confined. Fast ions have to be able to transfer their energy to the thermal plasma, and localized fast-ion losses from the plasma have to be avoided, as the heat fluxes associated with energetic-particle losses potentially can damage plasma facing components. Fast-ion confinement is a particular concern in stellarators, since without toroidal symmetry the confinement of fast ions is not guaranteed even if their initial orbits are small enough to lie within the confinement volume. To sufficiently confine fast ion at least in the plasma core, the optimization of

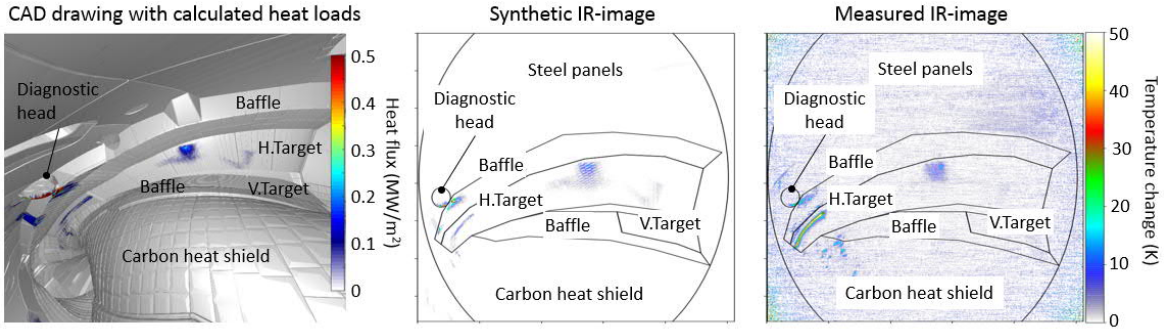

Figure 10. The figure compares expected and measured temperature changes induced by the heat fluxes from the fast ion losses (for the so-called high-iota configuration of W7-X and an NBI power of 3.5 MW). On the left side, the CAD representation of the in-vessel components is super-imposed with the calculated heat flux patterns from fast-ion losses using representative plasma temperature and density profiles. In the middle, the derived synthetic IR-image applying the power over 300 ms is shown (still with an arbitrary temperature scale, as the validation of the underlying plasma profiles and the exact NBI parameters is still ongoing). The plot on the right shows the measured temperature change (for plasma #20180822.20). In order to extract the effect of the fast ions, the measured IR-image consists of the difference between consecutive images with (after 300 ms) and without NBI.

W7-X relies on a quasi-isodynamic magnetic field configuration [65]. In such a configuration, the drifts of trapped particle orbits are mostly poloidal precession with only a small radial component, thus keeping the particles confined. However, the quasi-isodynamic configuration is only established at higher values of <β> requiring the contribution of the diamagnetic currents. This means that the optimization of the fast-ion confinement can only be verified once higher β-values are accessible. Since fast-ion confinement also depends on the chosen magnetic field configuration [66], this property could already be assessed during first W7-X experiments. A property which helps fast ion confinement in all magnetic field configurations (stellarators and tokamaks alike) is high plasma density, as it reduces the characteristic time scale for the collisional slowing down process (slowing-down time). Here, stellarators have an advantage over tokamaks, as the density limits usually exceed the Greenwald limit observed in tokamaks.

Verifying fast-ion confinement in a device like W7-X, which will not produce a significant amount of fast ions by fusion reactions, requires auxiliary sources of fast ions. There are two possibilities to generate fast ions, both of which are planned for W7-X. One is ion-cyclotron-resonance heating (ICRH) which is in preparation for future experiments [67]. The other one is neutral beam injection (NBI), which was applied to W7-X plasmas for the first time in the recent campaigns [68]. In W7-X, the NBI system produced neutral hydrogen beams with energies up to 55 keV and a power of up to 3.6 MW. After ionization by the plasma, the fast ions transfer their energy during a collisional slowing-down process. At these energies, the fast ion orbits are similar to those of the α-particles in a W7-X like fusion power plant. The characteristic quantity, which has to be comparable, is the ratio between the ion gyro-radius and the minor radius of the plasma, ρ/a (for 55 keV hydrogen at 2.5 T and a = 0.55 m, $\rho/a \approx$ 2.6%, while for 3.5 MeV helium at 5 T and a $\approx$ 2 m, $\rho/a \approx 2.7\%$).

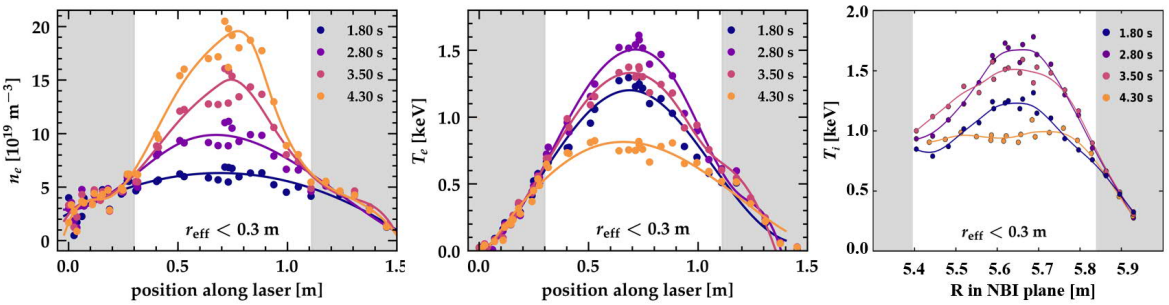

Figure 11. The different plots compare the temporal evolution of the profiles of electron density (from Thomson scattering), the electron temperature (from Thomson scattering), and the ion temperature (from CXRS). The profiles are plotted against the radii of respective diagnostics. The parts corresponding to a minor radius, r_{eff} < 0.3 m, are highlighted. Within this radius, the density gradients steepen and the central densities rises significantly above 10^{20} m^{-3}.

At W7-X, because of the limited space between the superconducting coils, the neutral beam injection geometry is nearly perpendicular to the toroidal field direction. This has the disadvantage that the parallel component of the initial velocity of the fast ions is small, preferentially populating those ion orbits, which immediately become trapped in the helical ripple of the magnetic field, resulting in elevated fast-ion losses [69]. For the first operation of the NBI, magnetic field configurations were chosen, based on the prediction of the smallest losses to critical in-vessel components. Using the fast-ion orbit following code, ASCOT [70], the analysis included all relevant details of in-vessel components including the front sides of plasma diagnostics. In one particular case, an optical diagnostic was fitted with a special protection collar to prevent fast ions hitting vacuum windows [71]. The main measurement for assessing the fast-ion losses used IR cameras, looking at particularly loaded areas. Figure 10 shows an example of such a measurement (for the high-iota magnetic field configuration), comparing predicted temperature changes due fast ion losses with IR-measurements. In order to remove the thermal heat loads from the image, the measurement shown is the difference between the IR images taken with and without fast-ion production, assuming that the thermal loads did not change in-between. As predicted, the highest fast ion heat fluxes are observed at or near the diagnostic head. Other hot spots can been seen at the left-hand side of the horizontal divertor target. The other areas receive much lower heat loads from fast ions. Overall, predicted and measured the fast-ion loss pattern agree very well, keeping in mind that the patterns depend on the chosen magnetic field configuration. Calculating the temperature changes caused by the fast ions using the ASCOT code for selected hot spots (using cases where IR-measurements show clear patterns and, at the same time, validated plasma profiles exist) and comparing them to the measured changes, they agree within a factor of two [72]. The observed deviations go in both directions (towards lower and higher fast ions losses), not indicating any systematic deviation between IR-measurements and fast-ion loss predictions. The preliminary conclusion is that the predicted losses of the fast ions produced by NBI, including the influence of the collisional slowing-down process, can be reproduced by the measurements, which is an important precondition for verifying fast-ion confinement at higher β.

An interesting observation, associated with applying NBI to W7-X plasmas, was a strong density peaking. Figure 11 illustrates the temporal evolution of density and temperature profiles. The corresponding plasma (20180919.033) was generated by applying 2 MW of ECRH. After ~1.5 s, ECRH was turned off and replaced by 3.4 MW of NBI (at 1.7 s). Not only did the density start to rise, but also

electron and ion temperatures (until 3.5 s), indicating a continuous improvement of the confinement during the NBI phase. This is supported by a marked increase of the plasma energy (measured by a diamagnetic loop) from ~0.3 to ~0.5 MJ. Only in the final phase of the plasma (after 3.5 s), when the central density approached values close to 2×10^{20} m^{-3}, did temperatures and energy drop again. During NBI, the observed density increase is achieved without gas fueling. Considering the particle fueling by NBI alone, the increase of the line-averaged density corresponds to a particle confinement time of several seconds, which is more than an order of magnitude above the energy confinement time. An important element of this analysis is a new charge-exchange recombination spectroscopy measurement, which was established together with NBI for measuring the ion temperature and low-Z impurity density profiles.

Low toroidal plasma currents and first island divertor operation

Preconditions for unproblematic island divertor operation are low toroidal plasma currents and a symmetric distribution of the heat loads between the ten divertor modules. The first aspect is linked to the optimization criterion minimizing the bootstrap current [6]. The dependence of the bootstrap current on the details of the magnetic field configuration was already confirmed during the first experimental campaign using a limiter configuration [73]. In the investigated configurations and at the investigated plasma parameters at low collisionality of the electrons, the relative change of the bootstrap current, when modifying the magnetic field, agreed with theoretical predictions. The specific absolute value of the bootstrap current was a factor of 3.5 smaller than in an equivalent tokamak (assuming the same pressure profile and aspect ratio), which demonstrates that the minimization of the bootstrap current works and the configuration can be considered as a way to control currents changing the rotational transform. Scaled to reactor relevant parameters, which has to include the effect of hot ions and the lower ι of actual tokamaks (the bootstrap current scales with $1/\iota$), the ratio between tokamak and stellarator bootstrap currents would further increase.

Although small (~10 kA), residual bootstrap currents can affect the magnetic islands. The bootstrap current forms on the time scale the plasma pressure builds up, screening currents prevent a fast increase of the total plasma current. This process takes place on the L/R time scale, which in W7-X is approximately 30 seconds. Thus, in plasmas with significant bootstrap current, the resonance condition for the magnetic island divertor slowly changes, moving the strike lines on the divertor targets [24]. To prevent heat loads reaching sensitive areas, several counter-measures are possible. One can introduce special protection elements, which take up the heat loads in case the strike lines move off the divertor targets. First tests with these “scraper-elements” [74] were successfully conducted in the past campaign. Another possibility is to control the strike line movement by ECCD. First investigations applying ECCD in the direction of the bootstrap current, anticipating the effect of the bootstrap current, or in counter-direction, compensating the bootstrap current, showed promising results [53]. However, there are also issues, which are related to the fact that localized ECCD produces low-order rational values of the rotation transform, which trigger instabilities, and that the current drive efficiency decreases with increasing plasma density.

The overall divertor performance strongly relies on a uniform heat load distribution over the ten divertor modules. The symmetry between the modules is affected by the alignment of the target tiles, magnetic field errors and also by plasma drift effects. For assessing the heat load distribution, W7-X is equipped with infra-red cameras looking at all ten divertor modules [75]. Figure 12 shows an example of such a measurement for the standard magnetic field configuration, which has $\iota = 1$ at the plasma

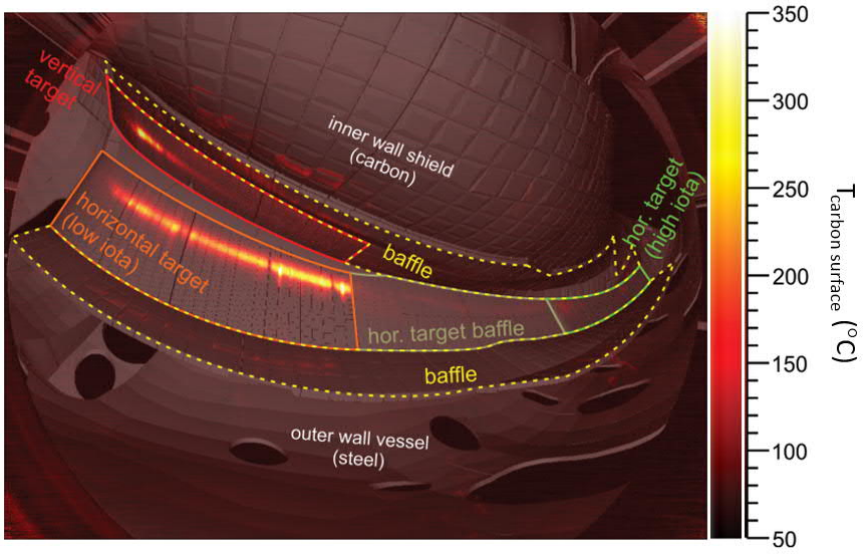

Figure 12. IR-image of one (of ten) divertor module superimposed with the CAD drawing of components inside the plasma vessel [76]. For comparison, see also Figure 4. The colour coding together with the scale on the right shows the temperature of carbon surfaces. The inscriptions refer to the different divertor and in-vessel components. In this example, using the standard magnetic field configuration, the main heat load in form of strike-lines is seen on the horizontal and vertical targets.

edge. Higher ι-values modify the edge magnetic islands, shifting the heat loads to the horizontal targets of the high-ι configuration. The measured heat-load distribution between the divertor modules shows relatively good alignment of the targets. In configurations that are not particularly sensitive to the 1/1 error fields (high- and low-ι), only one target (module 2) shows a larger deviation from the average load of ~20%. Comparing the asymmetries of these configurations with configurations in which the magnetic field direction was reversed showed an average up-/down asymmetry of 30% [76]. The influence of drifts on the up-/down symmetry of the heat load distribution is associated with the magnetic field gradient in a toroidal configuration. In the standard configuration with $\iota = 1$ at the plasma edge, which is sensitive to 1/1 error fields, the typical deviation from the mean value of the heat fluxes reaching divertor modules could be reduced to less than 30%, applying the trim coils with correct phase and amplitudes [76]. This means that in the standard configuration the asymmetries due to drift effects must be smaller than 30%. However, a detailed analysis of the up-/down asymmetries in the standard configuration is still missing. A first estimate, looking at the attached divertor phase of the plasma going into detachment (see Figure 13 below) indicates an up-/down asymmetry of ~15%.

A marked difference between the poloidal divertor in tokamaks and an the magnetic island divertor, as realized in W7-X, is the much longer field line connection lengths of the latter. Comparing ASDEX Upgrade with W7-X, the connection length of the open magnetic field lines in the scrape-off layer of the plasma increases from ~30 m to 300 m. Comparing ITER with a stellarator reactor, assuming a direct up-scaling from W7-X, the connection length values increase to 100 m and 1200 m, respectively [77]. The advantage of longer connection lengths is that the plasma, flowing along the open field lines to the divertor targets, can diffuse longer distances perpendicular to the magnetic field. This translates into a broader heat deposition profile on the targets. Thus, the divertor strike lines are expected to be

broader with lower peak heat fluxes. First experiments on W7-X confirm these expectations [22, 23]. A set of saddle coils located under the divertor targets (control coils) were used to directly modify the connections lengths. Applying coil currents, the connections lengths of the field lines hitting the targets at the position of the strike lines decreased from ~300 m to ~200 m. As a result, the width of the heat flux distribution dropped from ~10 cm to ~1 cm. At the same time, the peak heat flux rose by more than a factor of 1.6. For a complete comparison with the poloidal divertor, however, it has to be kept in mind that the strike-lines of the island divertor only cover certain areas in the helical direction, as can be seen in Figure 12. This is in contrast to the poloidal divertor, which distributes the heat over the complete toroidal circumference.

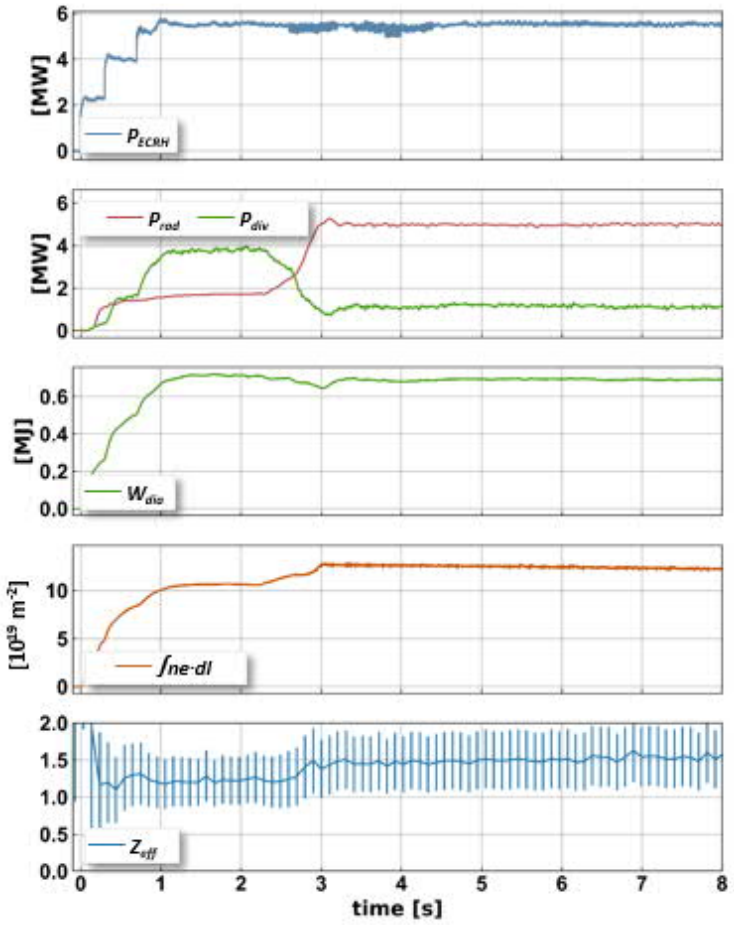

Figure 13. Divertor plasma developing full high-power detachment (#20181010.036). Shown are ECRH power (P_{ECRH}), diamagnetic energy (W_{dia}), line-integrated density ($\int n_e \cdot dl$), and the effective ion charge, Z_{eff} (inferred from bremsstrahlung). The drop of the power into the divertor (P_{div}) at t ≈ 2.2 s and the increase of the radiated power (P_{rad}) was triggered by introducing gas into the divertor region, clearly indicating divertor detachment. During detachment, all other plasma quantities stayed approximately constant.

Besides questions of heat flux distribution, a crucial question, in particular for the preparation of the long-pulse operation phase of W7-X, is the control of the overall heat flux reaching the divertor. When extrapolating to a power plant, it becomes clear that only a minor fraction of the heat leaving the plasma can be tolerated by the divertor [77]. A possible remedy is to radiate large fractions of the

heating power. The water-cooled high heat flux divertor of W7-X is designed for peak heat fluxes of 10 MW/m^2 [38], which, depending on the assumptions of the perpendicular heat diffusion in the scrape-off layer, corresponds to 10 MW of heating power if radiation losses are not included. In principle, this leaves a considerable margin for increasing the heating power or for the case that the assumptions about the heat flux distribution were not conservative enough. The divertor of the first operation periods of W7-X was uncooled, initially restricting the total energy per discharge to 80 MJ. Accordingly, the duration of typical plasmas was limited to 10 – 15 sec. At the end of the last campaign, an attempt was made to significantly increase plasma durations. To extend the permitted energy limit to 200 MJ, two types of plasma scenarios were developed.

The first was a plasma with 5 to 6 MW of ECRH power, using O2-heating to achieve high densities and the standard magnetic field configuration with an edge-ι of 1 (see Figure 13). To extend the pulse length, a density feedback scheme using a fast piezo valve hydrogen gas injector embedded directly by a divertor plate was applied. The line-averaged density was adjusted to a value close to 10^{20} m^{-3}. All relevant plasma quantities, including the effective ion charge, stayed roughly constant. The most striking observation is the sudden drop of the total power reaching the divertor, inferred from IR surface temperature measurements (in Figure 13 at t $\approx$ 2.2 s). As a consequence, the energy turnover of the longest plasmas could be easily raised to 150 MJ. In fact, the plasma duration was not limited by the divertor temperatures, but by problems with arc formation in the ECRH transmission line. The reduction of the heat fluxes onto the divertor targets is explained by a transition to a detached state, where most of the heating power is dissipated by radiation, distributing the heat over much larger areas. The tentative explanation assumes that a combination of high heating power and a moderate level of low-Z impurities leads to a higher density in the divertor region. This low-temperature, high-density plasma leads to an elevated radiation level and, at the same time, to neutral pressures between 5 and 8×10^{-4} mbar, which lies in the range required for effective pumping of the neutrals in the divertor region. Such high-power detachment was facilitated by the boronization of the plasma facing components, which significantly reduced the influx of low-Z impurities, in particular carbon and oxygen [78]. This is in contrast to low-power detachment, which was observed before boronization [79]. In this case, lower heating power and higher impurity levels move the radiation zone away from the divertor targets towards the plasma core, resulting in a radiating mantle surrounding the confinement region. In this scenario the neutral pressure in the divertor remained low (0.5×10^{-4} mbar) only achieving low neutral compression.

The second plasma approaching the energy limit of 200 MJ was heated with 2 MW of ECRH over 100 s. Despite the limited heating power, central temperatures of T_e = 2.5 keV and T_i = 1.8 keV and a central density of 3.8×10^{19} m^{-3} were achieved. Assuming a Z_{eff} = 1.5, the ion density is 90% of this value. Sustaining a plasma in W7-X over more than one minute, was also an important technical test verifying the long-pulse capability of the device.

Figure 14 summarizes the plasma performance of the first divertor operation phase of W7-X and compares the achieved values of the triple product to data originally compiled by [80]. To date, extending the plasma duartion always led to a lower performance. Causes for this limitation are limited cooling capacities of in-vessel components, heating and current drive systems which were not designed for long-pulse operation, normally conducting magnetc field coils as well as fundamental physics reasons. These include plasma operation close to stability limits or, for tokamaks, limitations of non-inductive current drive in the parameter range required for high performance operation. In W7-X, the change from limiter, ① [34], to divertor operation, which encompassed an increase of the

heating power and the energy limit, improved performance and pulse length. The duration of the highest performance plasma, ② [21, 53] was limited by the technical capabilities of the pellet injector. However, in this case investigations of plasma transport and stability are ongoing to also understand possible physical limitations. ③ corresponds to a 5 MW plasma with full divertor detachment ($n_{i0} \cdot T_{i0} \cdot \tau_E \approx 0.7\times10^{20}$ m^{-3} 2.0 keV 120 ms = 0.17×10^{20} m^{-3} keV s), which could be sustained for 30 s. Together with the 100 s 2 MW plasma, ④, the performance of these plasmas already approach the envelope of the whole data set.

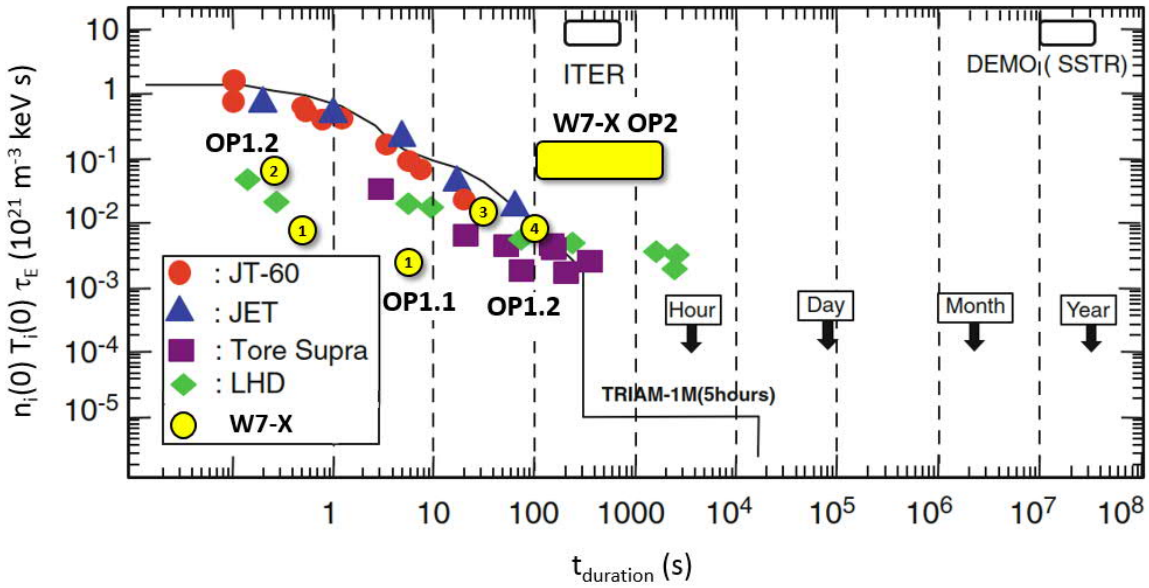

Figure 14. Comparison of the performance of first W7-X divertor plasmas with a large range of fusion experiments. The achieved triple products, derived from the central values of main ion density, ion temperature and energy confinement time, are plotted against the duration the triple product could be sustained. The numbering of the W7-X values correspond to different types of plasmas: ① represents a plasma achieved during W7-X limiter phase (OP1.1) [34]. ② is the highest triple product achieved in W7-X divertor plasmas (see Figure 6). ③ belongs to the 5 MW plasma which was sustained over 30 s. Finally, ④ corresponds to the 100 s, 2 MW plasma. This figure is an extended version of the figures in [21] and [34], originally based on work published in [80] (reproduced with the permission of Springer Nature).

Summary, conclusions and outlook

In preparation for steady-state operation, first W7-X divertor operation, using uncooled divertor targets, delivered many crucial results. Besides achieving a, for stellarators, record triple product, important studies were conducted concerning the magnetic island divertor, which is instrumental for achieving long-pulse or steady-state operation. Low intrinsic error field facilitated the equal distribution of the heat loads between the ten divertor modules. The minimization of the bootstrap current, which is one of the W7-X optimization criteria, could be quantitatively confirmed. Together with the verification of stable high-power detachment, this provides a good basis for the development of high-power steady-state plasmas. The envisaged parameter range for such plasmas is indicated in Figure 14 by the box marked “W7-X OP2”. The initial energy limit will be set to 1 GJ, corresponding to

100 s plasmas at a nominal power of 10 MW. The ultimate goal is to extend the pulse duration at this power level to 30 minutes.

An important ingredient for achieving high power detachment was the preceding glow discharge conditioning of the plasma vessel using an admixture of diborane. This significantly reduced the level of low-Z impurities.

First fast-ion heating and confinement studies were conducted taking the first lines of a neutral beam injection into operation. First results indicated that measurements are consistent with predicted fast-ion losses. The improvement of the fast ion confinement with increasing β-values, however, requires more heating power. An ICRH system, as an additional fast-ion source, the power deposition of which does not depend on the plasma density, is in preparation.

The main extension of W7-X is the installation of complete active (water) cooling of all plasma facing components, providing the technical basis for the development of high-power (~10 MW) long-pulse (up to 30 minutes) plasma scenarios. This, in particular, includes the installation of a high heat-flux (10 MW/m^2) divertor and cryogenic pumps for the divertor. Since plasma performance was limited by the heating power, a project will be started for developing higher power gyrotrons [81].

Acknowledgements

This work has been carried out within the framework of the EUROfusion Consortium and has received funding from the Euratom research and training programme 2014-2018 and 2019-2020 under grant agreement No 633053. The views and opinions expressed herein do not necessarily reflect those of the European Commission.

References

[1] P. Helander, C. D. Beidler, T.M. Bird, M. Drevlak, Y. Feng, R. Hatzky, F. Jenko, R. Kleiber, J.H.E. Proll, Yu. Turkin et al, Plasma Phys. Control. Fusion 54 (2012) 124009
[2] C. Gormezano, A. C. C. Sips, T. C. Luce, S. Ide, A. Becoulet, X. Litaudon, A. Isayama, J. Hobirk, M.R. Wade, T. Oikawa et al, Nucl Fusion 47 (2007) S285
[3] K. Ikeda, Nucl. Fusion 47 doi:10.1088/0029-5515/47/6/E01
[4] L. Spitzer, Phys. Fluids 1 (1958) 253
[5] M. Greenwald, Plasma Phys. Control. Fusion 44 (2002) R27
[6] C. D. Beidler, K. Allmaier, M.Yu. Isaev, S.V. Kasilov, W. Kernbichler, G.O. Leitold, H. Maaßberg, D. R. Mikkelsen, S. Murakami, M. Schmidt et al, Nucl. Fusion 51 (2011) 076001
[7] P. Helander, Rep. Prog. Phys. 77 (2014) 087001
[8] W. Wobig, S. Rehker, Proc. 7th Symp. on Fusion Techn., Grenoble, France (1972) 333
[9] M. Gasparotto, F. Elio, B. Heinemann, N. Jaksic, B. Mendelevitch, J. Simon-Weidner, B. Streibl, W7-X Team, Fusion Eng. Design 74 (2005) 161
[10] J. Nührenberg, W. Lotz, P. Merkel, C. Nührenberg, U. Schwenn, E. Strumberger, T. Hayashi, Fusion Techn. 27 (1995) 71
[11] G. Grieger, I. Milch, Phys. Bl. 49 (1993) 1001, doi.org/10.1002/phbl.19930491106
[12] M. Wanner, J.-H. Feist, H. Renner, J. Sapper, F. Schauer, H. Schneider, V. Erckmann, H. Niedermeyer, W7-X Team, Fusion Eng. Design 56-57 (2001) 155
[13] J. Geiger, C. D. Beidler, Y. Feng, H. Maaßberg, N.B. Marushchenko, Y. Turkin, Plasma Phys. Control. Fusion 57 (2015) 014004
[14] V. Erckmann, H. Braune, G. Gantenbein, J. Jelonnek, W. Kasparek, H.P. Laqua, C. Lechte, N. B. Marushchenko, G. Michel, B. Plaum et al, AIP Conf. Proc. 1580 (2014) 542
[15] T. Stange, H. P. Laqua, M. Beurskens, H.-S. Bosch, S. Bozhenkov, R. Brakel, H. Braune. K. J. Brunner, A. Cappa, A. Dinklage et al, EPJ Web of Conferences 157 (2017) 02008

[16] C. Lechte, W. Kasparek, B. Plaum, A. Zeitler, V. Erckmann, H. Laqua, N. Schneider, M. Weissgerber, A. Bechtold, M. Busch et al, EPJ Web of Conferences 147 (2017) 04004
[17] P. Grigull, K. McCormick, J. Baldzuhn, R. Burhenn, R. Brakel, H. Ehmler, Y. Feng, F. Gadelmeier, L. Giannone, D. Hartmann et al, Plasma Phys. Control. Fusion 43 (2001) A175
[18] M. Hirsch, J. Baldzuhn, C. Beidler, R. Brakel, R. Burhenn, A. Dinklage, H. Ehmler, M. Endler, V. Erckmann, Y. Feng et al, Plasma Phys. Control. Fusion 50 (2008) 053001
[19] H. Renner, J. Boscary, H. Greuner, H. Grote, F. W. Hoffmann, J. Kisslinger, E. Strumberger, B. Mendelevitch, Plasma Phys. Control. Fusion 44 (2002) 1005
[20] Y. Feng, M. Kobayashi, T. Lunt, D. Reiter, Plasma Phys. Control. Fusion 53 (2011) 024009
[21] T. Sunn Pedersen, R. König, M. Krychowiak, M. Jakubowski, J. Baldzuhn, S. Bozhenkov, G. Fuchert, A. Langenberg, H. Niemann, D. Zhang et al, Plasma Phys. Control. Fusion 61 (2019) 014035
[22] T. Sunn Pedersen, R. König, M. Jakubowski, Y. Feng, A. Ali, G. Anda, J. Baldzuhn, T. Barbui, C. Biedermann, B. Blackwell et al, 27th IAEA-FEC Ahmedabad (2018) EX/9-1 conferences.iaea.org/indico/event/151/contributions/6299/, submitted to Nucl. Fusion
[23] F. Effenberg, H. Niemann, Y. Feng, J. Geiger, O. Schmitz, Y. Suzuki, A. Ali, T. Barbui, S. Brezinsek, H. Frerichs et al, Nuclear Materials and Energy 18 (2019) 262
[24] J. Geiger, R. C. Wolf, C. Beidler, A. Cardella, E. Chlechowitz, V. Erckmann, G. Gantenbein, D. Hathiramani, M. Hirsch, W. Kasparek et al, Plasma Phys. Control. Fusion 55 (2013) 014006
[25] J. Kisslinger, T. Andreeva, Fusion Eng. Design 74 (2005) 623
[26] M. Jakubowski, A. Ali, P. Drewelow, Y. Gao, K. Hammond, H. Niemann, A. Puig Sitjes, F. Pisano, M. Sleczka, S. Brezinsek et al, 27th IAEA-FEC Ahmedabad (2018) EX/P8-16 conferences.iaea.org/indico/event/151/contributions/5790/
[27] S. A. Bozhenkov, M. Otte, C. Biedermann, M. Jakubowski, S.A. Lazerson, T. Sunn Pedersen, R. C. Wolf, W7-X Team, Nucl. Fusion 59 (2019) 026004
[28] T. Rummel, K. Rieße, F. Füllenbach, M. Köppen, J. Kißlinger, T. Brown, R. Hatcher, S. Langish, M. Mardenfeld, H. Neilson, IEEE Trans. Appl. Superconductivity 24 (2014) 4200904
[29] S.A. Lazerson, S. Bozhenkov, B. Israeli, M. Otte, H. Niemann, V. Bykov, M. Endler, T. Andreeva, A. Ali, P. Drewelow et al, Plasma Phys. Control. Fusion 60 (2018) 124002
[30] H.-S. Bosch, R.C. Wolf, T. Andreeva, J. Baldzuhn, D. Birus, T. Bluhm, T. Bräuer, H. Braune, V. Bykov, A. Cardella et al, Nucl. Fusion 53 (2013) 126001
[31] H.-S. Bosch, R. Brakel, T. Braeuer, V. Bykov, P. van Eeten, J.-H. Feist, F. Füllenbach, M. Gasparotto, H. Grote, T. Klinger et al, Nucl. Fusion 57 (2017) 116015
[32] R. C. Wolf, A. Ali, A. Alonso, J. Baldzuhn, C. Beidler, M. Beurskens, C. Biedermann, H.-S. Bosch, S. Bozhenkov, R. Brakel et al, Nucl. Fusion 57 (2017) 102020
[33] T. Klinger, A. Alonso, S. Bozhenkov, R. Burhenn, A. Dinklage, G. Fuchert, J. Geiger, O. Grulke, A. Langenberg, M. Hirsch et al, Plasma Phys. Control. Fusion 59 (2017) 014018
[34] T. Sunn Pedersen, A. Dinklage, Y. Turkin, R. C. Wolf, S. Bozhenkov, J. Geiger, G. Fuchert, H.-S. Bosch, K. Rahbarnia, H. Thomsen et al, Phys. Plasmas 24 (2017) 055503
[35] R. C. Wolf, C.D. Beidler, A. Dinklage, P. Helander, H. P. Laqua, F. Schauer, T. Sunn Pedersen, F. Warmer, W7X-Team, IEEE Trans. Plasma Science 44 (2016) 1466
[36] G. A. Wurden, C. Biedermann, F. Effenberg, M. Jakubowski, H. Niemann, L. Stephey, S. Bozhenkov, S. Brezinsek, J. Fellinger, B. Cannas et al, Nucl. Fusion 57 (2017) 056036
[37] A. Peacock, H. Greuner, F. Hurd, J. Kißlinger, R. König, B. Mendelevitch, R. Stadler, F. Schauer, R. Tivey, J. Tretter et al, Fusion Eng. Design 84 (2009) 1475
[38] J. Boscary, R. Stadler, A. Peacock, F. Hurd, A. Vorköper, B. Mendelevitch, A. Cardella, H. Pirsch, H. Tittes, J. Tretter et al, Fusion Eng. Design 86 (2011) 572
[39] J. Boscary, A. Peacock, T. Friedrich. H. Greuner, B. Böswirth, H. Tittes, W. Schulmeyer, F. Hurd, Fusion Eng. Design 87 (2012) 1453
[40] H.-S. Bosch, T. Andreeva, R. Brakel, T. Bräuer, D. Hartmann, A. Holtz, T. Klinger, H. Laqua, M. Nagel, D. Naujoks et al, IEEE Trans. Plasma Science 46 (2018) 1131
[41] M. Otte, D. Aßmus, C. Biedermann, S. Bozhenkov, T. Bräuer, A. Dudek, J. Geiger, G. Kocsis, S. Lazerson, T. Sunn Pedersen et al, Plasma Phys. Control. Fusion 58 (2016) 064003
[42] T. Sunn Pedersen, M. Otte, S. Lazerson, P. Helander, S. Bozhenkov, C. Biedermann, T. Klinger, R. C. Wolf, H.-S. Bosch, W7-X Team, Nat. Commun. 7 (2016) 13493
[43] S. A. Lazerson, M. Otte, S. Bozhenkov, C. Biedermann, T. Sunn Pedersen, W7-X Team, Nucl. Fusion 56 (2016) 106005
[44] S. A. Bozhenkov, S. Lazerson, M. Otte, D. A. Gates, T. Sunn Pedersen, R. C. Wolf, Nucl. Fusion 56 (2016) 076002

[45] H. Yamada, K. Kawahata, T. Mutoh, N. Ohyabu, Y. Takeiri, S. Imagawa, K. Ida, T. Mito, Y. Nagayama, T. Shimozuma et al, Fusion Sci. Techn. 58 (2010) 2010
[46] Y. Turkin, C.D. Beidler, H. Maaßberg, S. Murakami, V. Tribaldos, A. Wakasa, Phys. Plasmas 18 (2011) 022505
[47] C. D. Beidler, W. N. G. Hitchon, Plasma Phys. Control Fusion 36 (1994) 317
[48] S. Bozhenkov, A. Langenberg, C. Brandt, D. Zhang, E. Pasch, G. Kocsis, G. Wurden, G. Fuchert, H. Damm, H. P. Laqua et al, 27th IAEA-FEC Ahmedabad (2018) EX/P8-8 conferences.iaea.org/indico/event/151/contributions/ 5948/
[49] K.J. Brunner, T. Akiyama, M. Hirsch, J. Knauer, P. Kornejew, B. Kursinski, H. Laqua, J. Meineke, H. Trimino Mora, R. C. Wolf et al, JINST 13 (2018) P09002
[50] E. Pasch, M.N.A. Beurskens, S.A. Bozhenkov, G. Fuchert, J. Knauer, R. C. Wolf, W7-X Team, Rev. Sci. Instrum. 87 (2016) 11E729
[51] A. Langenberg, N. A. Pablant, O. Marchuk, D. Zhang, J. A. Alonso, R. Burhenn, J. Svensson, P. Valson, D. Gates, M. Beurskens et al, Nucl. Fusion 57 (2017) 086013
[52] K. Rahbarnia, H. Thomsen, U. Neuner, J. Schilling, J. Geiger, G. Fuchert, T. Andreeva, M. Endler, D. Hathiramini, T. Bluhm et al, Nucl. Fusion 58 (2018) 096010
[53] R. C. Wolf, S. Bozhenkov, A. Dinklage, G. Fuchert, Y. O. Kazakov, H. P. Laqua, S. Marsen, N. B. Marushchenko, T. Stange, M. Zanini et al, Plasma Phys. Control. Fusion 61 (2019) 014037
[54] H. Yamada, J. H. Harris, A. Dinklage, E. Ascasibar, F. Sano, S. Okamura, J. Talmadge, U. Stroth, A. Kus, S. Murakami et al, Nucl. Fusion 45 (2005) 1684
[55] T. Klinger, T. Andreeva, S. Bozhenkov, C. Brandt, R. Burhenn, B. Buttenschön, G. Fuchert, B. Geiger, O. Grulke, H.P. Laqua et al, Nucl. Fusion 59 (2019) 112004, doi.org/10.1088/1741-4326/ab03a7
[56] N. Pablant, A. Langenberg, A. Alonso, J. Baldzuhn, C.D. Beidler, L.G. Böttger, S. Bozhenkov, R. Burhenn, K. J. Brunner, A. Dinklage et al, 27th IAEA-FEC Ahmedabad (2018) EX/P8-31 conferences.iaea.org/indico/event/151/contributions/13126/
[57] N. Pablant, A. Langenberg, A. Alonso, C. D. Beidler, M. Bitter, S. Bozhenkov, R. Burhenn, M. Beurskens, L. Delgado-Aparicio, A. Dinklage et al, Phys. Plasmas 25 (2018) 022508
[58] M. Landreman, H.M. Smith, A. Mollén, P. Helander, Phys. Plasmas 21 (2014) 042503
[59] E. M. Edlund, M. Porkolab, Z. Huang, O. Grulke, L.-G. Böttger, C. von Sehren, A. von Stechow, Rev. Sci. Instrum. 89 (2018) 10E105
[60] T. Stange, H. P. Laqua, S. Bozhenkov, K.-J. Brunner, S. Marsen, D. Moseev, J. Baldzuhn, Y. O. Kazakov, U. Höfel, A. Langenberg, et al, to be submitted to Phys. Rev. Lett. (2019)
[61] G. Fuchert, J. Brunner, K. Rahbarnia, T. Stange, D. Zhang, J. Baldzuhn, S. A. Bozhenkov, C. D. Beidler, S. Brezinsek, R. Burhenn et al, 27th IAEA-FEC Ahmedabad (2018) EX/3-5 conferences.iaea.org/indico/event/151/contributions/5833/
[62] C. Nührenberg, Phys. Plasmas 3 (1996) 2401
[63] W. Park, D. A. Monticello, Nucl. Fusion 90 (1990) 2413
[64] E. Strumberger, S. Günter, Nucl. Fusion 57 (2017) 016032
[65] W. Lotz, P. Merkel, J. Nührenberg, E. Strumberger, Plasma Phys. Control Fusion 34 (1992) 1037
[66] M. Drevlak, J. Geiger, P. Helander, Y. Turkin, Nucl. Fusion 54 (2014) 073002
[67] J. Ongena, A. Messiaen, D. Van Eester, B. Schweer, P. Dumortier, F. Durodie, Ye. O. Kazakov, F. Louche, M. Vervier, R. Koch et al, Phys. Plasmas 21 (2014) 061514
[68] P. McNeely, M. Barlak, J. Baldzuhn, S. Bozhenkov, M. Drevlak, G. Gawlik, B. Heinemann, D. Holtum, J. Jagielski, R. Kairys et al, Fusion Eng. Design 88 (2013) 1034
[69] S. Äkäslompolo, M. Drevlak, Y. Turkin, S. Bozhenkov, T. Jesche, J. Kontula, T. Kurki-Suonio, R.C. Wolf, W7-X Team, Nucl. Fusion 58 (2018) 082010
[70] E. Hirvijoki, O. Asunta, T. Koskela, T. Kurki-Suonio, J. Miettunen, S. Sipilä, A. Snicker, S. Äkäslompolo, Comput. Phys. Commun. 185 (2014) 1310
[71] S. Äkäslompolo, P. Drewelow, Y. Gao, A. Ali, S. Bozhenkov, J. Fellinger, J. Geiger, D. Hartmann, D. Hathiramani, M. Jakubowski et al, Fusion Eng. Design (2019) doi.org/10.1016/j.fusengdes.2019.01.099
[72] S. Äkäslompolo, A. Ali, J. Baldzuhn, C. Biedermann, S. Bozhenkov, C. P. Dhard, P. Drewelow, M. Endler, J. Fellinger, O. Ford et al., to be submitted to J. Instrum. (2019)
[73] A. Dinklage, C. D. Beidler, P. Helander, G. Fuchert, H. Maaßberg, K. Rahbarnia, T. Sunn Pedersen, Y. Turkin, R. C. Wolf, A. Alonso et al, Nat. Phys. (2018) 14 855
[74] A. Lumsdaine, J. Boscary, J. Fellinger, J. Harris, H. Hölbe, R. König, J. Lore, D. McGinnis, H. Neilson, P. Titus et al, Fusion Eng. Design 98–99 (2015) 1357
[75] M. W. Jakubowski, P. Drewelow, J. Fellinger, A. Puig Sitjes, G. Wurden, A. Ali, C. Biedermann, B. Cannas, D. Chauvin, M. Gamradt et al, Rev. Sci. Instrum. 89 (2018) 10E116

[76] M. W. Jakubowski, A. Ali, P. Drewelow, Y. Gao, K. Hammond, H. Niemann, A. Puig Sitjes, F. Pisano, M. Sleczka, S. Brezinsek et al, 27th IAEA-FEC Ahmedabad (2018) EX/P8-16 conferences.iaea.org/indico/event/151/contributions/5790/
[77] Y. Feng, J. Nucl. Mat. 438 (2013) S497
[78] T. Wauters, A. Goriaev, A. Alonso, J. Baldzuhn, R. Brakel, S. Brezinsek, A. Dinklage, H. Grote, J. Fellinger, O. Ford et al, Nucl. Mat. and Energy 17 (2018) 235
[79] D. Zhang, R. König, Y. Feng, R. Burhenn, S. Brezinsek, M. Jakubowski, B. Buttenschön, H. Niemann, M. Krychowiak, A. Alonso et al, submitted to Phys. Rev. Lett. (2019)
[80] M. Kikuchi, M. Azumi, Frontiers in Fusion Research II (Introduction to Modern Tokamak Physics) figure 3.16 and appendix in ch 3 (Berlin: Springer), 2015
[81] K. A. Avramidis, T. Ruess, F. Mentgen, J. Jin, D. Wagner, G. Gantenbein, S. Illy C. Ioannidis, H. P. Laqua, I. G. Pagonakis et al, EPJ Web Conf. 203 (2019) 04003